

Remote epitaxy and exfoliation of vanadium dioxide via sub-nanometer thick amorphous interlayer

Received: 22 August 2024

Accepted: 11 December 2024

Published online: 02 January 2025

 Check for updates

Chang Liu^{1,2,7}, Xing Li^{1,2,7}, Yang Wang^{1,2,7}, Zhi Zheng^{1,2}, Binmin Wu³,
Wenhao He⁴, Xiang Dong^{1,2}, Ziyu Zhang^{1,2}, Bingxin Chen⁵, Jiayuan Huang^{1,2},
Zhenghua An⁵, Changlin Zheng⁴, Gaoshan Huang^{1,2} &
Yongfeng Mei^{1,2,6} ✉

The recently emerged remote epitaxy technique, utilizing 2D materials (mostly graphene) as interlayers between the epilayer and the substrate, enables the exfoliation of crystalline nanomembranes from the substrate, expanding the range of potential device applications. However, remote epitaxy has been so far applied to a limited range of material systems, owing to the need of stringent growth conditions to avoid graphene damaging, and has therefore remained challenging for the synthesis of oxide nanomembranes. Here, we demonstrate the remote epitaxial growth of an oxide nanomembrane (vanadium dioxide, VO₂) with a sub-nanometer thick amorphous interlayer, which can withstand potential sputtering-induced damage and oxidation. By removing the amorphous interlayer, a 4-inch wafer-scale freestanding VO₂ nanomembrane can be obtained, exhibiting intact crystalline structure and physical properties. In addition, multi-shaped freestanding infrared bolometers are fabricated based on the epitaxial VO₂ nanomembranes, showing high detectivity and low current noise. Our strategy provides a promising way to explore various freestanding heteroepitaxial oxide materials for future large-scale integrated circuits and functional devices.

Epitaxy^{1,2}, a method to grow high-crystallized nanomembrane on a single crystallographic oriented wafer, has already been a popular way to realize multi-functional electronic and photonic devices^{3–6}. Compared with homoepitaxy, the heteroepitaxy^{5,6}, being capable of growing epitaxial nanomembrane on dissimilar substrates owing to near lattice-matching, opens a wide range of preparation of high-quality functional oxides exhibiting intriguing phenomena, such as

ferroelectricity, superconductivity and metal-insulator-transition (MIT)^{7–11}. However, the traditional heteroepitaxy of oxide has some self-limitations that hinder its further manipulation. The lattice mismatch between the epitaxial nanomembrane and the substrate introduces strain generation and the chemical bonding between the two materials poses a challenge for the releasing, these factors lead to stringent limitations in achieving optimal performance and

¹Department of Materials Science & International Institute of Intelligent Nanorobots and Nanosystems, State Key Laboratory of Surface Physics, Fudan University, Shanghai 200438, People's Republic of China. ²Yiwu Research Institute of Fudan University, Yiwu 322000 Zhejiang, People's Republic of China. ³State Key Laboratory of Infrared Physics, Shanghai Institute of Technical Physics, Chinese Academy of Sciences, Shanghai 200083, People's Republic of China. ⁴State Key Laboratory of Surface Physics and Department of Physics, Fudan University, Shanghai 200433, People's Republic of China. ⁵State Key Laboratory of Surface Physics & Institute for Nanoelectronic Devices and Quantum Computing, Department of Physics, Fudan University, Shanghai 200438, People's Republic of China. ⁶Shanghai Frontiers Science Research Base of Intelligent Optoelectronics and Perception, Institute of Optoelectronics, Fudan University, Shanghai 200438, People's Republic of China. ⁷These authors contributed equally: Chang Liu, Xing Li, Yang Wang. ✉ e-mail: yfm@fudan.edu.cn

heterogeneous integration of the oxide-based device^{3,12}. Therefore, it is urgent to seek a method for releasing and transferring the epitaxial oxide nanomembrane to meet the demand of diverse applications.

Some techniques have been employed previously to overcome this challenge^{13–15}. 2D material-assisted epitaxy, including van der Waals epitaxy (vdW epitaxy)^{16–18} and remote epitaxy^{19–21}, is an emerging method in which the 2D material (especially graphene) is utilized as the substrate or inserted layer between epilayer and substrate. Due to zero dangling bonds and weak vdW force at the graphene surface^{16,22}, the epilayer can detach from substrate easily after epitaxial growth^{23–25}. These epitaxial methods enrich facilitate exfoliation of epitaxial films (e.g., III-V semiconductors) from the substrate^{12,26–29}. However, the graphene is susceptible to harsh growth environments (e.g., oxidation and plasma) and transfer process^{30,31}, leading to the limitation of remote epitaxy in preparation of large-scale freestanding epitaxial oxides. Although some improvements are implemented such as multilayers graphene or defective hBN replacing the monolayer graphene^{12,29}, epitaxial films are mainly focused on III-V semiconductors that utilize milder growth methods, thus the applicable materials are still restricted.

Here, we demonstrate a practical remote epitaxy and exfoliation method of preparing wafer-scale freestanding oxides NM via sub-nanometer amorphous Al₂O₃ grown by atomic layer deposition (ALD) as the interlayer. The key point of this method is the ALD technique, holding the advantage of self-termination^{32,33}, where we can control the thickness of interlayer precisely (from one atomic layer to hundreds of nanometers) by adjusting the ALD growth cycles. The sub-nanometer thick amorphous Al₂O₃ interlayer will not screen the electrostatic potential from substrate and also not crystallize with the upper oxide layer. Moreover, the amorphous Al₂O₃ is robust enough to withstand the harsh growth environments like oxidation and bombardment, and can be removed by HF easily as the sacrificial layer. In views of this, the wafer-scale epitaxial vanadium dioxide nanomembrane (VO₂ NM) grown by reactive sputtering with the amorphous Al₂O₃ as interlayer can be exfoliated from sapphire and transferred to various substrates. The as-grown VO₂ NM exhibits nearly single-crystalline characteristic³⁴ (i.e., it has a single out-of-plane orientation and threefold in-plane orientation) and 4 orders of magnitude of resistance change during MIT. Last, multi-shaped (e.g., exfoliated, buckled and rolled-up) infrared bolometers based on freestanding epitaxial VO₂ NMs show higher blackbody detectivity and lower current noise comparing to the polycrystalline VO₂ NMs. Our finding extends the remote epitaxy methods and enriches the freestanding epitaxial oxide nanomembrane family greatly, and consequently provides a promising route to fabricate advanced devices in electronics and photonics.

Results

Remote epitaxial growth of VO₂ NM via ALD technique

To investigate whether the remote epitaxy could realize with the participation of amorphous materials, Fig. 1a illustrates the atomic configuration with amorphous Al₂O₃ interlayer on sapphire substrate simulated by density functional theory (DFT) (detailed see Supplementary Note 1 and Supplementary Fig. 1). The charge density (ρ) distribution is calculated and can be seen on the surface of amorphous Al₂O₃ from the plane-view in Fig. 1b. To observe the ρ transferred from the substrate clearly, cross-sectional ρ distribution is studied along the (11 $\bar{2}$ 0) plane (Fig. 1c) which reveals that partial charge can transfer to the top surface of amorphous Al₂O₃ interlayer, and its period distribution reveals that the electrostatic potential from substrate is not totally screened by amorphous Al₂O₃ interlayer. Based on the simulation, we experimentally verify the feasibility of remote epitaxial growth of VO₂ NM with amorphous Al₂O₃ interlayer which is schematically shown in Fig. 1d. A uniform and ultra-thin amorphous Al₂O₃ interlayer is firstly deposited by ALD, followed by growing VO₂ NM epitaxially through reactive sputtering. Afterwards, the as-grown VO₂ NM can be lifted off by removing the amorphous Al₂O₃ interlayer and transferred

to arbitrary substrate (Supplementary Fig. 2). Figure 1e and Supplementary Fig. 3 demonstrate the cross-sectional scanning transmission electron microscopy (STEM) images of as-grown VO₂ NM showing dense and uniform crystal grain without pinhole at the interlayer, implying the remote epitaxial growth instead of lateral overgrowth epitaxy at pinhole^{35–37}. Further by atomically resolved high-angle annular dark-field (HAADF) STEM, the VO₂ epilayer can be observed clearly, aligning well with the sapphire substrate through the amorphous Al₂O₃ created by ALD which is visible between the epitaxial layer and the substrate (indicated by the dash line in Fig. 1f). The atomic configurations of VO₂ and sapphire are in consistent with the simulation of corresponding crystal axis. The fast Fourier transform (FFT) and convergent beam electron diffraction (CBED) (Supplementary Fig. 4) of VO₂ epilayer and sapphire display clear diffraction pattern, confirming the excellent crystallization. Last, a uniform 4-inch VO₂ NM is successfully prepared (Supplementary Fig. 5) and after wet-etching the amorphous Al₂O₃ interlayer, the wafer-scale freestanding epitaxial VO₂ NM can be obtained as shown in Fig. 1g and Supplementary Fig. 6. To investigate if the graphene can participate as the interlayer, we also sputter VO₂ NM on graphene and the results show that the graphene is damaged probably owing to the bombardment from the sputtering (Supplementary Fig. 7). It is manifested that the amorphous materials as interlayer via ALD technique is feasible to obtain wafer-scale freestanding epitaxial oxide nanomembrane^{38–42}.

Interlayer of optimization for improving epitaxial quality

In order to investigate the effect of ALD interlayer thickness to epitaxy, we prepare amorphous Al₂O₃ interlayer of different thicknesses by altering the ALD cycles from 0 to 200 (Supplementary Fig. 8 and Supplementary Fig. 9) and confirm that the VO₂ NMs epitaxial growth can be kept with the interlayer thickness of up to 10 ALD cycles, and the DFT calculations also confirm the thickness effect (Supplementary Fig. 10). Therefore, the samples with 0, 5, 8 and 10 ALD cycles interlayer are selected for detailed discussion in Fig. 2. From the cross-sectional STEM images in Fig. 2a–d, the interlayers grow thicker with the increase of ALD growth cycles. The corresponding X-ray diffraction (XRD) ϕ -scans of as-grown VO₂ (011) peak in Fig. 2e–h show that there are six peaks of VO₂ NM and the peak intensity is decreasing with increase of ALD growth cycles. This result indicates that the thicker is the interlayer, the less electrostatic potential can affect the epilayer atoms arranging on the substrate. The charge density of the amorphous Al₂O₃/Al₂O₃ substrate, as determined by DFT calculations, further confirms that increasing the interlayer thickness significantly impacts the periodic potential on the surface (Supplementary Fig. 11). The electron backscatter diffraction (EBSD) shown in Fig. 2i–l also confirm this phenomenon from which we can identify a single out-of-plane orientation belonging to b-axis [010] of VO₂. Besides, the interlayer thickness will also induce the strain change of as-grown VO₂ NMs as shown in Fig. 2m–p and Supplementary Fig. 12 reciprocal space mapping (RSM). Similar regularities are observed in VO₂ NMs of different thicknesses (Supplementary Fig. 13) and atomic-resolution image of the VO₂-substrate interface (Supplementary Fig. 14). The VO₂ peak moves downward and approaches the bulk VO₂ value gradually even the peak intensity is a little weaker for the sample with Al₂O₃ interlayer of 10 ALD cycles. Accordingly, we calculate the average strain change based on the Q_z (see Supplementary Fig. 15) and observe that the strain decreases from 0.422% to 0.024% with the interlayer thickness increasing. This indicates that the thicker amorphous Al₂O₃ interlayer not only weakens the epitaxial performance (as in the case of interlayer with 15 ALD cycles illustrated in Supplementary Fig. 16) but also serves to relax the out-of-plane epitaxial strain³⁸. The strain states also can be reflected by the MIT temperature demonstrated in Supplementary Fig. 17. When the VO₂ grows on sapphire directly (0 ALD cycle), the c-axis is under a tensile stress which will lift the MIT temperature, and with the lattice relaxation, the MIT temperature moves towards the lower value. Though thinner interlayer can maintain the VO₂ NM a better crystal

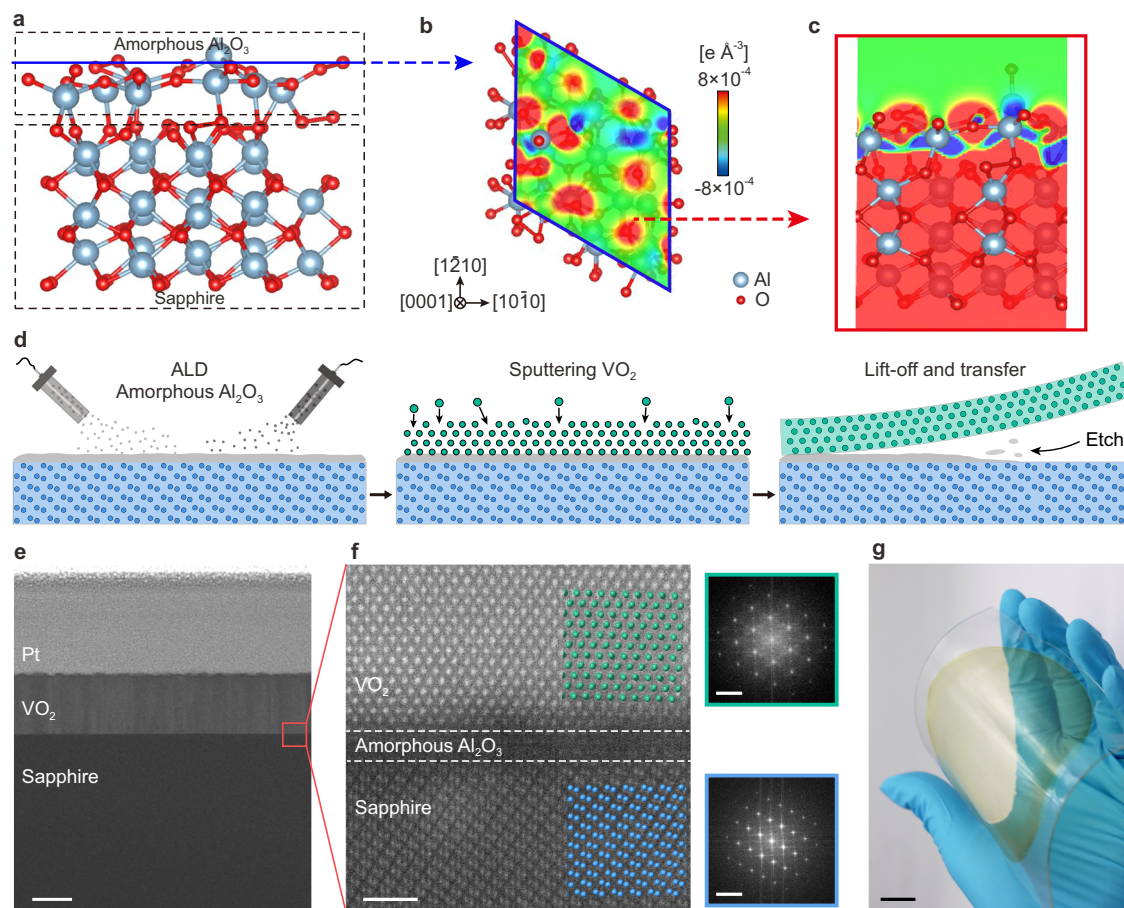


Fig. 1 | Remote epitaxial growth of VO₂ nanomembrane (NM) via atomic layer deposition (ALD) technique. **a** Atomic structure configuration of amorphous Al₂O₃ interlayer on sapphire substrate in density functional theory (DFT) calculation. **b** Plan-view charge density (ρ) contour map of the top surface of amorphous Al₂O₃ interlayer indicated in **(a)** with blue line. **c** The cross-sectional ρ distribution contour map. **d** Process schematic of remote epitaxial growth of VO₂ NM. ALD is used to form the amorphous Al₂O₃ interlayer on sapphire (0001) substrate, followed by growing VO₂ NM epitaxially through reactive sputtering. Finally, the as-grown VO₂ NM can be lifted off and transferred by etching away the amorphous

Al₂O₃ interlayer. **e** Cross sectional scanning transmission electron microscopy (STEM) image of as-grown VO₂ NM on sapphire substrate. The scale bar is 100 nm. **f** High-angle annular dark-field (HAADF)-STEM image of the interface area between VO₂ NM and sapphire substrate, corresponding to the square showed in **(e)**, scale bar is 1 nm. The insets are simulated atomic configurations of VO₂ NM and sapphire. The right panels are the respective fast Fourier transform (FFT) of VO₂ NM and sapphire, scale bar is 5 nm⁻¹. **g** Photograph of transferred 4-inch epitaxial VO₂ NM on polyimide/polydimethylsiloxane (PI/PDMS). Scale bar is 2 cm.

quality but it also induces island morphology (Supplementary Fig. 18) probably owing to the nature of ALD growth mechanism and sputtering bombardment³³. Meanwhile, the lift-off process for thinner interlayer samples will be difficult because epilayer and substrate cannot be completely separated (Supplementary Fig. 19).

In addition to the interlayer thickness, the interlayer material is also studied. We replace the amorphous Al₂O₃ with crystallized ZnO or HfO₂. However, the as-grown VO₂ NMs become polycrystalline even interlayers are only 10 ALD cycles. And the XRD peak intensity of VO₂ NMs with 5 ALD cycles ZnO or HfO₂ interlayer drop strongly compared to the amorphous Al₂O₃ interlayer (Supplementary Fig. 20). It indicates that the crystallized interlayer blocks the charge transfer from the substrate than the amorphous Al₂O₃ interlayer even under a thin thickness, which is consistent with the DFT simulation results (Supplementary Fig. 21). Therefore, it's better to choose amorphous Al₂O₃ rather than ZnO or HfO₂ as interlayer for our remote epitaxy method.

Epitaxial orientation analysis of VO₂ NM

For the as-grown VO₂ NM, the epitaxial relation between sapphire substrate is elucidated comprehensively in Fig. 3. The pole figure and φ -scan (Fig. 3a and Supplementary Fig. 22) shows that sapphire exhibits three-fold symmetry along the [0001] orientation which is the

normal orientation of the sapphire substrate (0001). But for VO₂ NM, it is noteworthy that despite the monoclinic structure's [010] orientation exhibiting two-fold symmetry, there are six distinct (011) peaks each separated by 60°. Furthermore, no additional diffraction peaks are observed within a 90° χ angle.

Though some works analyzed the epitaxy of VO₂ nanowire, there is a little controversy about this phenomenon in VO₂ NM according to previous reports^{43–45}. To explore the epitaxial relation, cross-sectional STEM is conducted with a wide view from sapphire [2 $\bar{1}$ 10] axis (Fig. 3b–d) and the results show two distinct atomic configurations of VO₂: [102] and [201] axes. And the zoomed-in atomic configurations in the insets of Fig. 3c and d are consistent with the simulations. It's very reasonable to extrapolate that the VO₂ possesses rotational three-fold symmetry in plane, which means that the epitaxial relation is VO₂ [102] or [201] paralleling with sapphire [2 $\bar{1}$ 10] as illustrated in Fig. 3e schematically. To verify this assumption, we also analyze another crystal axis (sapphire [10 $\bar{1}$ 0] in Supplementary Fig. 23) and find that the corresponding VO₂ atomic configurations match well with the simulations as expected. Herein, we can preliminarily conclude that there are three equivalent directions separated by 120° distributing in plane randomly. Another crystal plane (220) is checked by φ -scan shown in Supplementary Fig. 24 which confirms the epitaxial relation again.

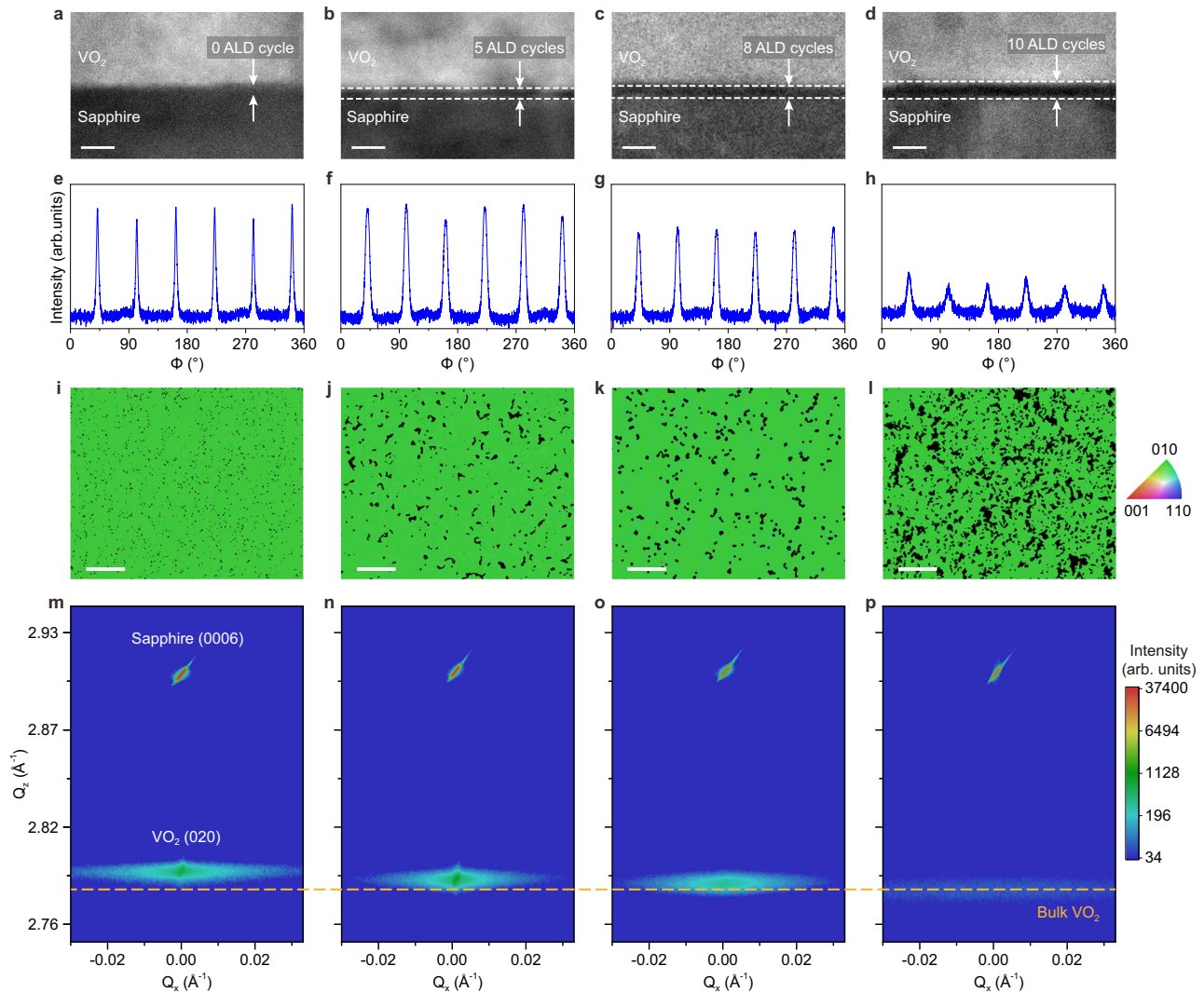


Fig. 2 | Effect of the thickness of ALD amorphous interlayer to remote epitaxial property of as-grown VO₂ NM. From left to right column: epitaxial VO₂ NMs grown on sapphire substrate with amorphous Al₂O₃ interlayer of 0, 5, 8 and 10 ALD cycles. **a–d** Cross sectional STEM images. The dash lines indicate the amorphous Al₂O₃ interlayer. Scale bars: 5 nm. **e–h** X-ray diffraction (XRD) ϕ -scan of VO₂ (011) peak,

showing six peaks for all as-grown VO₂ NM samples. **i–l** Electron backscatter diffraction (EBSD) mapping. All as-grown VO₂ samples demonstrate single out-of-plane orientation. Scale bars: 2 μ m. **m–p** Reciprocal space mapping (RSM) around VO₂ (020) peak. The yellow line indicates the Q_z position of bulk VO₂.

Benefiting from this remote epitaxy we proposed, the plane-view observation can be obtained by transferring the VO₂ NM from sapphire to the TEM grid (Fig. 3f). The single VO₂ [010] domains with in-plane mis-orientation can be distinguished clearly in Fig. 3g. More interestingly, from Fig. 3h and Supplementary Fig. 25, the selected area electron diffraction (SAED) pattern displays hexagon lattice which results from the diffraction of out-of-plane growth direction (VO₂ [010]) but rotating 120° in plane. Based on the analysis above, the VO₂ NM has the nearly single-crystalline characteristic, i.e., it has a single out-of-plane orientation and three equivalent in-plane orientations.

Comparison of as-grown and transferred VO₂ NM

After dissolving the amorphous Al₂O₃ interlayer and transferring the freestanding epitaxial VO₂ NM (transferred VO₂ NM), there is a crucial question that whether the transferred VO₂ NM could be robust enough to withstand the HF etching. Here we take the VO₂ NM with 8 ALD cycles interlayer for transfer as an example. Firstly, we check the surfaces of VO₂ NMs before and after transferring using AFM (Supplementary Fig. 26) which shows undamaged morphology of transferred VO₂ NM. Furthermore, the epitaxial quality is confirmed by XRD 2θ - ω scan and rocking

curve (Fig. 4a) which shows that the transferred VO₂ NM still displays a single diffraction peak and the FWHM almost remains same. And the XRD ϕ -scan also shows six (011) peaks as as-grown VO₂ NM (Fig. 4b). To obtain more detailed information about the crystal structures of transferred VO₂ NM, the out-of-plane lattice parameters are monitored by RSM around the (020) reflection plane (Fig. 4c). The data show intense reflection peak, signifying the well crystallization. Besides, compared to the as-grown VO₂ NM, the transferred VO₂ NM peak moves downward, which is understandable because the strain is relaxed after transferring and thus the lattice distance along b-axis gets longer. Moreover, in Fig. 4d, temperature-dependent resistance reveals that the resistance modulation across MIT can be ~ 4 orders of magnitude after the wet-etching which is the benchmark of high-quality VO₂ NM in reported researches⁴⁶, and the MIT temperature gets closer to 68 °C after releasing the VO₂ NM from substrate since the strain in VO₂ NM get relaxed without the substrate effect. Further analysis using Raman spectroscopy (Fig. 4e and Supplementary Fig. 27) shows that all Raman peaks belong to the monoclinic phase of VO₂, confirming the undamaged transferred VO₂ NM. It's convincible to conclude that the crystal structure and property remain intact after the wet etch process.

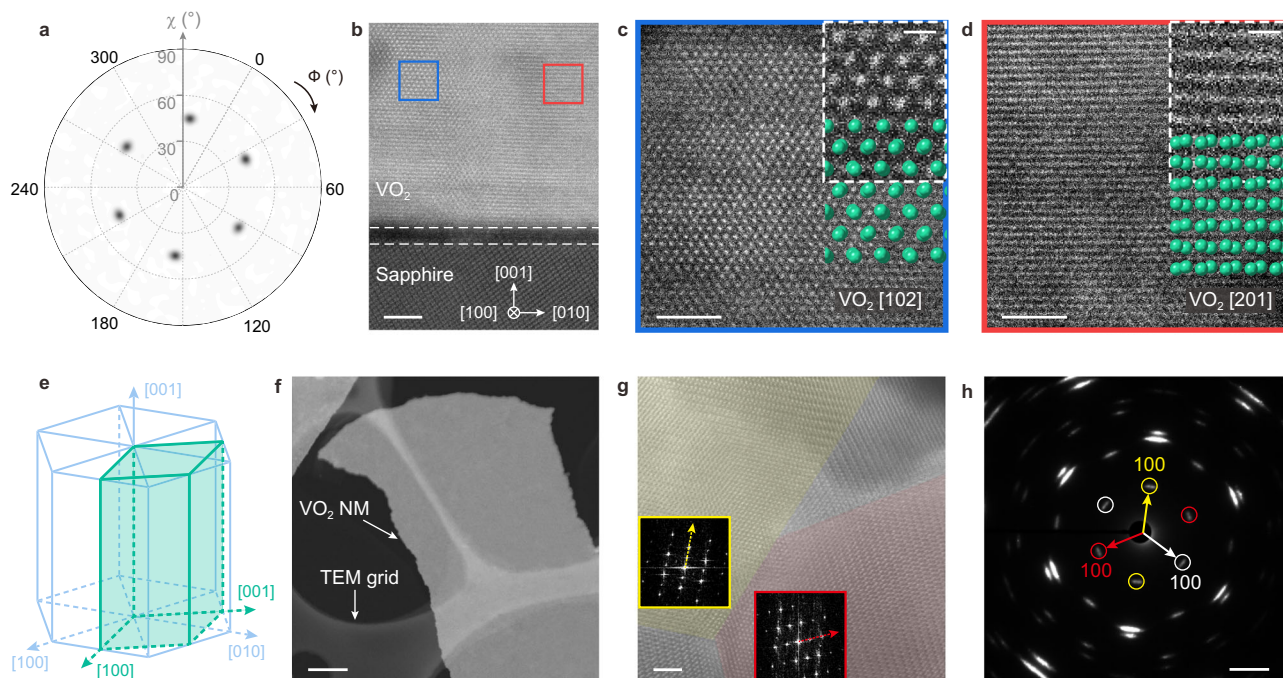


Fig. 3 | Epitaxial orientation analysis of VO₂ NM. **a** XRD pole-figure of VO₂ (011) plane. **b** Cross sectional STEM image of VO₂ NM and sapphire (zone axis is sapphire [2110]). Scale bar: 5 nm. HAADF-STEM images of different VO₂ domains indicated by red and blue squares are shown in (c) and (d) respectively (zone axis: VO₂ [102] and [201]). And the insets denoted by white dashed boxes (zoomed-in atomic images) are consistent with the simulations. Scale bars: 2 nm. **e** Schematic of epitaxial relation between VO₂ (green) and sapphire (blue). **f** STEM image of

transferred VO₂ NM on TEM grid (Scale bar: 1 μm). **g** Out-of-plane HAADF-STEM image of VO₂ domains (Scale bar: 2 nm) indicated by red and yellow shades. The insets show FFT images and the arrow direction is VO₂ [100]. **h** Plane-view selected area electron diffraction (SAED) image of transferred VO₂ NM showing in-plane three-fold symmetry, scale bar is 2 nm⁻¹. The out-of-plane direction is VO₂ [010] zone axis.

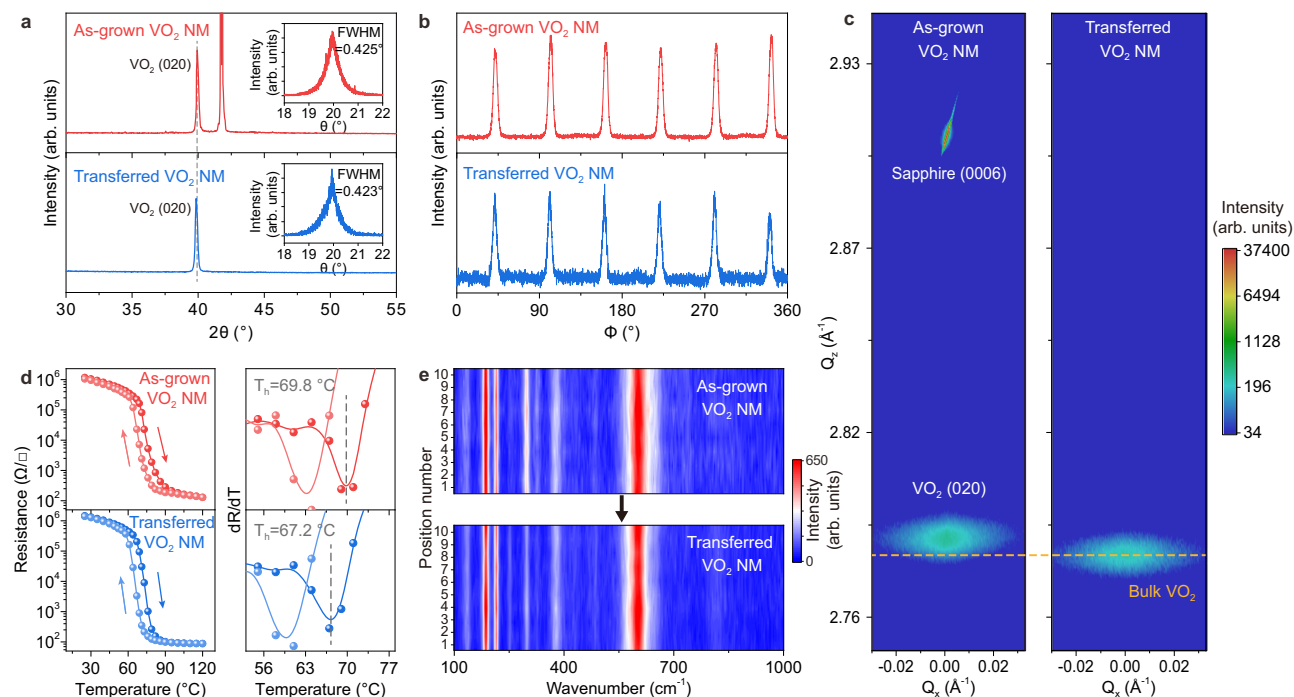


Fig. 4 | Characterization of as-grown and transferred VO₂ NM. **a** XRD 2θ-ω scan (Insets: rocking curves of as-grown and transferred VO₂ NMs). **b** XRD φ-scan of VO₂ (011) plane. **c** RSM at around VO₂ (020) peak. The yellow dash line indicates the bulk VO₂ value. These show single out-of-plane orientation and in-plane three-fold symmetry of both as-grown and transferred VO₂ NM. **d** Left: temperature-

dependent resistance change in heating and cooling cycle, showing 4 orders of magnitude of modulation. Right: first derivative of resistance to show the metal-insulator-transition (MIT) temperature (T_h). **e** Raman spectra obtained along a line scanning of the VO₂ NM (~10 μm) which confirm the monoclinic phase of both as-grown and transferred VO₂ NM (The arrow represent the transfer process).

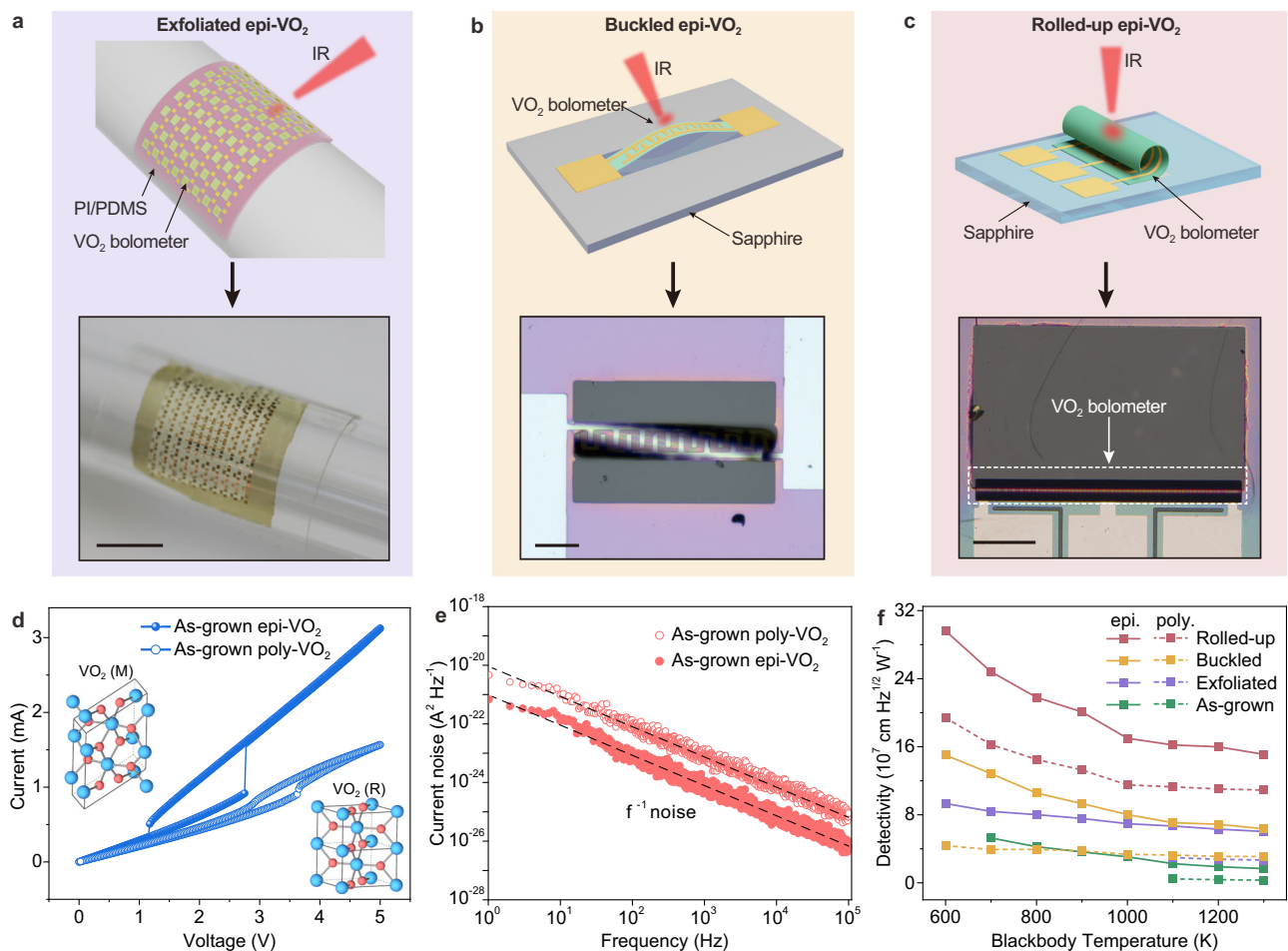


Fig. 5 | Multi-shape VO₂ NM bolometers. **a** Exfoliated epi-VO₂ bolometer. Scale bar: 1 cm. **b** Buckled epi-VO₂ bolometer. Scale bar: 100 μm. **c** Rolled-up epi-VO₂ bolometer. The diameter of microtube is ~50 μm. Scale bar: 200 μm. The upper in (a–c) are schematic illustrations of device and the lower are optical images of the practical samples. **d** I–V characteristics of as-grown epi-VO₂ and poly-VO₂ bolometers in dark environment and at room temperature. The epi-VO₂ bolometer

shows higher current response. Insets: Schematic crystal structure of VO₂ monoclinic (M) and rutile (R) phase. **e** Current noise of as-grown epi-VO₂ and poly-VO₂ bolometers varied with frequency. The epi-VO₂ bolometer shows lower current noise. The dash lines represent the tendency of f⁻¹ noise. **f** Detectivity versus blackbody temperature of different devices under 2 V bias. (The epi- and poly- refer to epitaxial and polycrystalline VO₂ NM respectively).

Multi-shape freestanding VO₂ NM bolometers

After exfoliation, three types of infrared bolometers fabricated using freestanding epitaxial VO₂ NMs (epi-VO₂) are illustrated in Fig. 5a–c to demonstrate the possibility of infrared detection (detailed preparation processes are described in Supplementary Figs. 28–32 and Methods), and for comparison, similar bolometers based on polycrystalline VO₂ NMs (poly-VO₂) were also fabricated. The electrical properties of these bolometers are characterized by I–V curves in Fig. 5d and Supplementary Fig. 33. With the voltage increasing from 0 to 5 V, the VO₂ changes from monoclinic phase to rutile phase as the generated Joule heat leads to elevated temperature. To further estimate noise sources of bolometers, the current noise is measured and the results (Fig. 5e and Supplementary Fig. 34) exhibit that 1/f noise is the main noise source and the noise of poly-VO₂ bolometers is stronger than epi-VO₂ bolometers owing to the irregular crystal orientation which will enhance the electrons scattering from the grain boundary. In order to explore the application ability, the blackbody is used as a radiation source to simulate the infrared detection environment. The detectivity of the four types of bolometers based on epi- and poly-VO₂ NMs are shown in Fig. 5f. The exfoliated VO₂ bolometer consisting of epi-VO₂ NM/PI/PDMS shows flexible property and the detectivity is higher than the as-grown epi-VO₂ owing to the lower thermal conductivity of PI/PDMS. By buckling the epi-VO₂/PI layer to isolate bolometer, the detectivity can be elevated further because the air surrounding the buckled epi-VO₂ bolometer localizes the heat caused by

irradiation of IR light. The last type uses the stress engineering to roll the VO₂ NM into a multi-turns microtube. Since the microtube has multi-layers walls, the most heat is absorbed by VO₂ instead of spreading to the substrate. Therefore, the performance is greatly improved in rolled-up epi-VO₂ bolometer and the detectivity can reach $2.96 \times 10^8 \text{ cm Hz}^{1/2} \text{ W}^{-1}$, which is much higher than the values from literature and commercial devices summarized in Supplementary Fig. 35^{47,48}. Moreover, it is worth noting that for each type the bolometer made by the poly-VO₂ NMs shows worse detection performance compared with the epi-VO₂ bolometers. It is revealed that the better and ordered crystallization will induce better detective performance. Besides the bolometer, some other applications such as radiative cooling device and rolling actuator are also shown in Supplementary Figs. 36 and 37. These various types of VO₂ devices can be further integrated with micro-electronics depending on the application scenarios and expand the application potentials.

Discussion

In summary, we provide a practical strategy to produce freestanding epitaxial oxide nanomembrane by remote epitaxy. The key point of this technique is growing uniform amorphous interlayer with sub-nanometer thickness by using ALD which holds the advantage of self-termination and shape conformality. The charge from substrate can transfer to the top surface of the interlayer to arrange the atoms in epilayer. More significantly, the interlayer prepared by ALD can

withstand harsh growth environment so that more growth techniques of complex oxide can be adopted. For example, we prepared epitaxial 150-nm-VO₂ NM by reactive sputtering with the existence of amorphous Al₂O₃ interlayer (~8 Å) on sapphire. The as-grown VO₂ NM performs uniform epitaxial alignment and the freestanding VO₂ NM is still intact after release and transfer process, demonstrating excellent resistance modulation as high as 10⁴. Apart from this, we also prepare epitaxial VO₂ NMs on TiO₂ (100) substrate successfully by this approach (Supplementary Fig. 38). Finally, multi-shape bolometers are fabricated based on the epitaxial VO₂ NM, which show higher detectivity ($2.96 \times 10^8 \text{ cm Hz}^{1/2} \text{ W}^{-1}$) than that of commercial devices.

We envision that the ALD technique makes the remote epitaxy possible to adapt diverse growth conditions, and thus greatly enrich the kinds of epitaxial oxides. This approach can be extended further by developing new amorphous materials as sacrificial layer. It also offers the practical opportunities to not only realize novel heterostructure and flexible optoelectronic device, but also study interfacial physics and electronics.

Methods

DFT calculation

The DFT as implemented in the Vienna Ab initio simulation package (VASP) was employed in all calculations. The generalized gradient approximation of Perdew-Burke-Ernzerhof (GGA-PBE) was used to describe the exchange-correlation potential. The projector augmented-wave (PAW) method was employed to treat interactions between ion cores and valence electrons and the plane-wave cutoff energy was fixed to 400 eV. All given structural models were optimized until the Hellmann-Feynman forces smaller than -0.01 eV/\AA and the change in energy smaller than 10^{-5} eV was attained. Further details and discussion are given in Supplementary Note 1.

Epitaxial film growth

The 4-inch c-plane sapphire substrate (Microcrystalline Semiconductor Materials (Suzhou) Co., Ltd.) was used as substrate and cleaned 20 min by acetone, ethanol and DI water before growth. Then, the interlayer (amorphous Al₂O₃, crystallized ZnO and HfO₂) were deposited by ALD (MNT Micro and Nanotech Co., Ltd.). The chamber base pressure was 10 Pa and temperature is set to 200 °C. For amorphous Al₂O₃ growth, the precursors were TMA (pulse time: 20 ms, purge time: 20 ms) and DI water (pulse time: 20 ms, purge time: 25 ms), and the growth rate is -0.11 nm/cycle . For HfO₂ growth, the precursors were TDMAH (pulse time: 200 ms, purge time: 15 ms) and DI water (pulse time: 20 ms, purge time: 20 ms) with the growth rate is -0.122 nm/cycle . For ZnO growth, the precursors were DEZ (pulse time: 20 ms, purge time: 15 ms) and DI water (pulse time: 25 ms, purge time: 20 ms) with the growth rate is -0.12 nm/cycle .

Then, the substrate was loaded into PVD chamber (Kurt J. Lesker, PVD 75) with base vacuum of -10^{-6} Torr , and the VO₂ NM (~150 nm) was grown by reactive sputtering for 1500 s (DC power: 100 W, target: V metal, gas flow: Ar 60 sccm and O₂ 5 sccm). The substrate holder temperature rose to 550 °C and was rotating at speed of 10 rpm while growing to ensure the film uniformity. After the growth of VO₂, the sample was cooled down to room temperature and taken out from the chamber.

XRD, EBSD, Raman spectroscopy and resistance measurement

High-resolution XRD was performed by Bruker D8 Advance with Cu K_{α1} radiation ($\lambda = 0.15406 \text{ nm}$). The detailed information about out-of-plane lattice parameters and in-plane epitaxial relationship and strain states were obtained by symmetric 2θ - ω scan, ϕ -scan, pole figure and RSM mapping. The EBSD mapping measurements were made using JEOL JSM 7200 F equipped with EDAX Velocity Super detector with post-noise reduction.

Raman spectroscopy (Renishaw inVia-Qontor) mapping was obtained by scanning ten dots along a line. The resistance versus temperature plot was conducted with temperature-controlled stage (CRYOX-MINI, PSAIC, China) and four-point resistance test system (HPS2663, Helpass Electronic Technologies, Inc.). For 4-inch VO₂ NM measurement, we selected 21 points on the surface shown in Supplementary Fig. 39.

TEM measurement

Two sample types were prepared for plane-view imaging of transferred VO₂ NM on a TEM grid and cross-sectional imaging of VO₂/amorphous Al₂O₃/sapphire. For the plane-view observation, after selective removing of the Al₂O₃ interlayer, the VO₂ NM was naturally released and attached to the TEM grid shown in Supplementary Fig. 40. TEM lamella was prepared by focused ion beam (Helios G4 UX, Thermo Fisher Scientific Inc.) with Ga⁺ ion beam thinning by using the standard lift-out method for cross-section viewing. TEM and STEM imaging were performed to examine the thin film morphology and atomic structure near the interface of VO₂/amorphous Al₂O₃/sapphire. The sample was characterized by a field-emission TEM (Themis Z, Thermo Fisher Scientific) fitted with double aberration correctors (SCORR and CETCOR, CEOS GmbH) operated at 300 kV. For HAADF STEM imaging, the semi-convergence angle of 21.4 mrad and collection angle of 79-200 mrad were used. The out-of-plane view was characterized by a field-emission TEM (JEM ARM200F, JEOL) equipped with a probe aberration corrector (CS CORRECTOR, CEOS GmbH) operated at 200 kV.

Release and transfer of VO₂ NM and fabrication of VO₂ bolometers

The exfoliation process of remote-epitaxial VO₂ NM is shown in Supplementary Fig. 28. The PI is spin-coated onto the VO₂ surface by spin coater (KW-4A, SIYOUYEN Ltd.). The as-grown VO₂ NM was coated with HMDS (90 °C, 20 min) to enhance binding force with PI. After coating, the film was loaded in oven for heat cure. Then the whole film was immersed into 40% HF to remove the amorphous Al₂O₃. Finally, the freestanding epitaxial VO₂ NM can be obtained. The etching rate of amorphous Al₂O₃ and epitaxial VO₂ is illustrated in Supplementary Fig. 29. The exfoliation process of polycrystalline VO₂ NM grown on Si/SiO₂ substrate is the same as for the that of remote-epitaxial VO₂ NM. After coating HMDS and PI, the whole film was immersed into 40% HF to remove the SiO₂. The freestanding poly-VO₂ NM can be obtained.

The fabrication process of exfoliated epi-VO₂ bolometer is shown in Supplementary Fig. 30. The epi-VO₂/PI bilayer and poly-VO₂/PI (exfoliation from Si/SiO₂ substrates) bilayer are flipped and put on a bare Si substrate. The film-on-Si was spin-coated with photoresist (AZ5214, Microchemicals GmbH, Germany) and exposed with device array using lithography (Microwriter ML3, Durham Magneto Optics Ltd.). After development, the uncovered area was dry-etched by using reactive ion etching (RIE-10NR, Samco Inc.), followed by washing the photoresist with acetone. Then, the metal electrode deposition was carried out using e-beam evaporation (Lab 18, Kurt J. Lesker). Finally, the exfoliated VO₂ can be taken off the Si substrate and transferred to PDMS finally.

The fabrication process of buckled epi-VO₂ bolometer is shown in Supplementary Fig. 31. The patterned epi-VO₂ or poly-VO₂ areas were exposed by lithography, and dry-etching the uncovered area by RIE, followed by metal deposition (e-beam) to form the electrodes on both sides of the VO₂ NM. Then wet-etching the amorphous Al₂O₃ or SiO₂ by HF, the VO₂ NMs were buckled up from the substrate.

The fabrication process of rolled-up epi-VO₂ bolometer is shown in Supplementary Fig. 32. The patterned epi-VO₂ or poly-VO₂ areas were exposed by lithography, and dry-etching the uncovered area by RIE, followed by metal deposition (e-beam) to form the electrodes on one side of the VO₂ NM. Then wet-etching the amorphous Al₂O₃ or SiO₂

by HF, the VO₂ NM would roll up to a microtube due to the internal strain difference.

For the as-grown VO₂ bolometer. The VO₂/sapphire with the amorphous Al₂O₃ interlayer and VO₂ grown on Si/SiO₂ substrate were spin-coated with photoresist and exposed with device array using lithography. After development, the uncovered area was dry-etched by using reactive ion etching, followed by washing the photoresist with acetone. Then, the metal electrode deposition was carried out using e-beam evaporation.

Optoelectronic measurements

The devices were placed in a vacuum Dewar with pressure of 10⁻⁴ Pa. The measurement of photocurrent of blackbody was carried out with a calibrated commercial blackbody furnace from 600 K to 1300 K under 2.0 V bias. The frequency was modulated by an optical chopper wheel, and the photocurrent signal was collected by (Keysight B2902B). The photo response measurement was carried out with a modulated laser beam and the photocurrent signal was acquired by an oscilloscope (TBS2000, Tektronix) and a current amplifier (Stanford SR570).

Data availability

The Source Data underlying the figures of this study are available with the paper. All raw data generated during the current study are available from the corresponding authors upon request. Source data are provided with this paper.

References

- Bauer, E. & Poppa, H. Recent advances in epitaxy. *Thin Solid Films* **12**, 167–185 (1972).
- Cho, A. Y. & Arthur, J. R. Molecular beam epitaxy. *Prog. Solid State Chem.* **10**, 157–191 (1975).
- Du, L. et al. Moiré photonics and optoelectronics. *Science* **379**, eadg0014 (2023).
- Abel, S. et al. A strong electro-optically active lead-free ferroelectric integrated on silicon. *Nat. Commun.* **4**, 1671 (2013).
- Chen, Y. et al. Strain engineering and epitaxial stabilization of halide perovskites. *Nature* **577**, 209–215 (2020).
- Ren, J., Segal-Peretz, T., Zhou, C., Craig, G. S. W. & Nealey, P. F. Three-dimensional superlattice engineering with block copolymer epitaxy. *Sci. Adv.* **6**, eaaz0002 (2020).
- Yuan, R. et al. A calibratable sensory neuron based on epitaxial VO₂ for spike-based neuromorphic multisensory system. *Nat. Commun.* **13**, 3973 (2022).
- Bai, L. et al. Pressure-induced phase transitions and metallization in VO₂. *Phys. Rev. B* **91**, 104110 (2015).
- Liu, M. K. et al. Anisotropic electronic state via spontaneous phase separation in strained vanadium dioxide films. *Phys. Rev. Lett.* **111**, 096602 (2013).
- Martin, L. W. & Rappe, A. M. Thin-film ferroelectric materials and their applications. *Nat. Rev. Mater.* **2**, 16087 (2016).
- Ohtomo, A. & Hwang, H. Y. A high-mobility electron gas at the LaAlO₃/SrTiO₃ heterointerface. *Nature* **427**, 423–426 (2004).
- Kum, H. S. et al. Heterogeneous integration of single-crystalline complex-oxide membranes. *Nature* **578**, 75–81 (2020).
- Bedell, S. W. et al. Layer transfer by controlled spalling. *J. Phys. D: Appl. Phys.* **46**, 152002 (2013).
- Lu, D. et al. Synthesis of freestanding single-crystal perovskite films and heterostructures by etching of sacrificial water-soluble layers. *Nat. Mater.* **15**, 1255–1260 (2016).
- Wong, W. S., Sands, T. & Cheung, N. W. Damage-free separation of GaN thin films from sapphire substrates. *Appl. Phys. Lett.* **72**, 599–601 (1998).
- Bakti Utama, M. I. et al. Recent developments and future directions in the growth of nanostructures by van der Waals epitaxy. *Nanoscale* **5**, 3570–3588 (2013).
- Geim, A. K. & Grigorieva, I. V. Van der Waals heterostructures. *Nature* **499**, 419–425 (2013).
- Kim, J. et al. Principle of direct van der Waals epitaxy of single-crystalline films on epitaxial graphene. *Nat. Commun.* **5**, 4836 (2014).
- Kim, Y. et al. Remote epitaxy through graphene enables two-dimensional material-based layer transfer. *Nature* **544**, 340–343 (2017).
- Kong, W. et al. Polarity governs atomic interaction through two-dimensional materials. *Nat. Mater.* **17**, 999–1004 (2018).
- Kim, H. et al. Remote epitaxy. *Nat. Rev. Methods Prim.* **2**, 40 (2022).
- Rafiee, J. et al. Wetting transparency of graphene. *Nat. Mater.* **11**, 217–222 (2012).
- Bae, S.-H. et al. Graphene-assisted spontaneous relaxation towards dislocation-free heteroepitaxy. *Nat. Nanotechnol.* **15**, 272–276 (2020).
- Dai, L. et al. Highly heterogeneous epitaxy of flexoelectric BaTiO_{3-δ} membrane on Ge. *Nat. Commun.* **13**, 2990 (2022).
- Liu, B. et al. Atomic mechanism of strain alleviation and dislocation reduction in highly mismatched remote heteroepitaxy using a graphene interlayer. *Nano Lett.* **22**, 3364–3371 (2022).
- Kum, H. et al. Epitaxial growth and layer-transfer techniques for heterogeneous integration of materials for electronic and photonic devices. *Nat. Electron.* **2**, 439–450 (2019).
- Jeong, J. et al. Remote heteroepitaxy of GaN microrod heterostructures for deformable light-emitting diodes and wafer recycle. *Sci. Adv.* **6**, eaaz5180 (2020).
- Jiang, J. et al. Carrier lifetime enhancement in halide perovskite via remote epitaxy. *Nat. Commun.* **10**, 4145 (2019).
- Zhou, G. et al. Superior quality low-temperature growth of three-dimensional semiconductors using intermediate two-dimensional layers. *ACS Nano* **16**, 19385–19392 (2022).
- Kim, H. et al. Role of transferred graphene on atomic interaction of GaAs for remote epitaxy. *J. Appl. Phys.* **130**, 174901 (2021).
- Kim, H. et al. Impact of 2D–3D heterointerface on remote epitaxial interaction through graphene. *ACS Nano* **15**, 10587–10596 (2021).
- Miikkulainen, V., Leskelä, M., Ritala, M. & Puurunen, R. L. Crystallinity of inorganic films grown by atomic layer deposition: Overview and general trends. *J. Appl. Phys.* **113**, 021301 (2013).
- Puurunen, R. L. Surface chemistry of atomic layer deposition: A case study for the trimethylaluminum/water process. *J. Appl. Phys.* **97**, 121301 (2005).
- Ren, F. et al. Van der Waals epitaxy of nearly single-crystalline nitride films on amorphous graphene-glass wafer. *Sci. Adv.* **7**, eabf5011 (2021).
- Chang, C. S. et al. Remote epitaxial interaction through graphene. *Sci. Adv.* **9**, eadj5379 (2023).
- Du, D. et al. Controlling the balance between remote, pinhole, and van der Waals epitaxy of heusler films on graphene/sapphire. *Nano Lett.* **22**, 8647–8653 (2022).
- Kim, H. et al. Graphene nanopattern as a universal epitaxy platform for single-crystal membrane production and defect reduction. *Nat. Nanotechnol.* **17**, 1054–1059 (2022).
- Guo, Y. et al. A reconfigurable remotely epitaxial VO₂ electrical heterostructure. *Nano Lett.* **20**, 33–42 (2019).
- Lee, D. K. et al. Heterogeneous integration of single-crystalline rutile nanomembranes with steep phase transition on silicon substrates. *Nat. Commun.* **12**, 5019 (2021).
- Li, X. et al. Epitaxial liftoff of wafer-scale VO₂ nanomembranes for flexible, ultrasensitive tactile sensors. *Adv. Mater. Technol.* **4**, 1800695 (2019).
- Ma, H. et al. Wafer-scale freestanding vanadium dioxide film. *Sci. Adv.* **7**, eabk3438 (2021).
- Kim, H. et al. Flexible thermochromic window based on hybridized VO₂/graphene. *ACS Nano* **7**, 5769–5776 (2013).

43. Fan, L. L. et al. Oxygen pressure dependent VO₂ crystal film preparation and the interfacial epitaxial growth study. *Thin Solid Films* **520**, 6124–6129 (2012).
44. Fu, D. et al. Comprehensive study of the metal-insulator transition in pulsed laser deposited epitaxial VO₂ thin films. *J. Appl. Phys.* **113**, 043707 (2013).
45. Zhou, H., Chisholm, M. F., Yang, T.-H., Pennycook, S. J. & Narayan, J. Role of interfacial transition layers in VO₂/Al₂O₃ heterostructures. *J. Appl. Phys.* **110**, 073515 (2011).
46. Zhang, H.-T. et al. Wafer-scale growth of VO₂ thin films using a combinatorial approach. *Nat. Commun.* **6**, 8475 (2015).
47. Wu, B. et al. One-step rolling fabrication of VO₂ tubular bolometers with polarization-sensitive and omnidirectional detection. *Sci. Adv.* **9**, eadi7805 (2023).
48. Hyseni, G., Caka, N. & Hyseni, K. Infrared thermal detectors parameters: semiconductor bolometers versus pyroelectrics. *WSEAS Trans. Cir. Sys.* **9**, 238–247 (2010).

Acknowledgements

This work is supported by the National Natural Science Foundation of China (62375054, Y. M. Nos. 523B2107, Z. Zhang), Science and Technology Commission of Shanghai Municipality (24520750200, Y. M., 24CL2900200, Y. M.), and Shanghai Talent Programs. Part of the experimental work was carried out in Fudan Nanofabrication Laboratory. The computations in this research were performed using the CFFF platform of Fudan University.

Author contributions

Yongfeng Mei conceived the idea and led the research. C. Liu conducted the nanomembrane growth, XRD characterization, Raman spectroscopy. X. Li conducted the lift-off and transfer process, and bolometer fabrication with the assistance of Z. Zhang. DFT calculations were conducted by C. Liu and Y. Wang. The TEM characterization was conducted by C. Zheng, W. He, and Z. Zheng. Raman spectroscopy was conducted with the assistance of J. Huang and X. Dong. The characterization of bolometer was conducted by C. Liu, B. Wu, B. Chen and Z. An. And G. Huang, Y. Mei, and X. Li co-wrote the paper. X. Li, B. Wu, and Y. Wang discussed the results and gave advice on figures and manuscript.

Competing interests

The authors declare no competing interests.

Additional information

Supplementary information The online version contains supplementary material available at <https://doi.org/10.1038/s41467-024-55402-8>.

Correspondence and requests for materials should be addressed to Yongfeng Mei.

Peer review information : *Nature Communications* thanks Kai Liu and the other, anonymous, reviewer for their contribution to the peer review of this work. A peer review file is available.

Reprints and permissions information is available at <http://www.nature.com/reprints>

Publisher's note Springer Nature remains neutral with regard to jurisdictional claims in published maps and institutional affiliations.

Open Access This article is licensed under a Creative Commons Attribution-NonCommercial-NoDerivatives 4.0 International License, which permits any non-commercial use, sharing, distribution and reproduction in any medium or format, as long as you give appropriate credit to the original author(s) and the source, provide a link to the Creative Commons licence, and indicate if you modified the licensed material. You do not have permission under this licence to share adapted material derived from this article or parts of it. The images or other third party material in this article are included in the article's Creative Commons licence, unless indicated otherwise in a credit line to the material. If material is not included in the article's Creative Commons licence and your intended use is not permitted by statutory regulation or exceeds the permitted use, you will need to obtain permission directly from the copyright holder. To view a copy of this licence, visit <http://creativecommons.org/licenses/by-nc-nd/4.0/>.

© The Author(s) 2024